Chemically Stable Tetrazine-Based Porous Organic Cages with Post-Synthetic Modification via iEDDA Reactions

Ju Yang[1], Saisai Yu[1], Wendi Zhang[1], Dingyue Hu[1,2], Yutao Guan[1], Hongqin Li[1,2], Ming Liu[1,2*]

[1] Department of Chemistry, Zhejiang University, Hangzhou 310027.

[2] Hangzhou Global Scientific and Technological Innovation Center (HIC), Zhejiang University, Hangzhou 311200

*Corresponding Authors: mingliu@zju.edu.cn

KEYWORDS: Porous organic cages, tetrazine, chemical stability, post-synthetic modification, iEDDA Reactions.

ABSTRACT: Porous organic cages (POCs) have emerged as promising porous materials for a wide range of applications. However, their development is often limited by insufficient chemical stability and challenges in systematically functionization. Herein, we reported the design and synthesis of a tetrazine-based POC (**TC1**) with rigid tetrahedral structures via a one-pot nucleophilic aromatic substitution reaction. **TC1** exhibits high porosity, with a BET surface area at 1157 m^2/g, and remarkable chemically stability, retaining its integrity even in concentrated acid. Its well-defined cavity size and electron-deficient environment enable effective SF_6/N_2 separation, as confirmed by dynamic breakthrough experiments. Post-synthetic modification of **TC1** via inverse electron-demand Diels-Alder (iEDDA) reactions yielded two functionalized cages (**TC2** and **TC3**), which maintain good porosity and display further enhanced chemical stability over a broad pH range (-1 to 15). Furthermore, cage-based networked materials (**TC1-P1** and **TC1-P2**) were successfully constructed through the iEDDA polymerization using **TC1** as building unit, resulting in tunable porous frameworks with improved CO_2/N_2 selectivity.

INTRODUCTION

Porous Organic Cages (POCs) are an emerging subclass of porous materials consist of discrete molecules with intrinsic cavities[1, 2]. They offer unique advantages, including good processability and structural modularity[2-4], which complement those of crystalline porous materials. POCs have shown great promise in applications such as precision separation, energy storage, chemical sensing, and catalysis[5-8], Despite the progress made since their first report in 2009[9], two major challenges continue to hinder the further development and boarder application of these promising materials: insufficient chemical stability and limited structural diversity.

First, most shape-persistent POCs reported to date have been assembled via dynamic covalent chemistry, such as imine[9, 10] or boronic ester condensation[11, 12]. As a result, many of these structures are prone to decomposition under acidic or basic condition, or even upon exposure to atmosphere humidity. To address this issue, efforts have been made to construct POCs with irreversible bond-forming chemistry, including amidation reactions for forming amide bonds[13, 14], Knoevenagel condensation reactions for forming carbon-carbon bonds[15], and aromatic nucleophilic substitution reactions for forming carbon-oxygen bonds[16, 17]. However, bypassing reversible bond formation in self-assembly process often comes at the cost of reduced designability and compromised shape-persistence. Consequently, only a few of POCs formed by irreversible bonds have been reported to exhibit good porosity[15, 18]. Second, it remains challenging to systematic tune the POC structures by predesigning the building block, in contrast to extended frameworks. Even subtle changes in the building blocks can significantly affect the self-assembly products. To circumvent this, post-synthetic modification (PSM) strategy has been explored to introduce functional groups that are otherwise difficult to incorporate directly. However, successful examples of PSM on POCs remain limited. Notable cases include the "molecular tying" strategy, which stabilizes imine bonds by converting them into five-membered aminal rings[19] and the "pinnick oxidation" reaction[20], which transforms imines to amides. From an application perspective, ideal POCs should exhibit high porosity, robust chemical stability, and facile post-synthetic functionalization—though the latter two attributes often present a trade-off. Therefore, there is an ongoing demand for the design and synthesis of POCs that simultaneously achieve chemical robustness and functionalizability.

Nucleophilic aromatic substitution (S_NAr) reactions are widely employed in the construction of functionalized aromatic systems and have been successfully applied to the synthesis of supramolecular architectures, including macrocycles and POCs[21-23]. From the chemical reaction standpoint, electron-deficient aromatic rings are particularly susceptible to S_NAr reactions, with nucleophilic reactivity increasing as the electron deficiency of the ring intensifies. Electron-poor compounds—such as meta-dihalogenated pyridines, triazines, tetrazines, and their derivatives—exhibit high S_NAr reactivity due to their low electron density[24-26]. For example, Xu et al. efficiently synthesized [2+4] POCs based on electron-deficient pyridine derivatives via a one-pot S_NAr reaction, enabling the construction of cage-based assemblies[27]. Cooper's group reported a larger [4[2+3]+6] cage formed via S_NAr between triazine chlorides and phenols, which exhibited good gas adsorption properties[18], although the synthesis required relatively complex building blocks. Tetrazine has also proven to be a promising scaffold for cage construction via S_NAr reactions. For instance, the Carrillo group successfully synthesized a tetrazine-based cage using this approach, though its porosity and other physical properties in solid state were not further investigated[28]. These precedents suggest that S_NAr reactions involving tetrazines offer an efficient strategy for constructing POCs. More importantly, the electron-deficient nature of tetrazine renders its highly amenable to structural diversification via inverse electron-demand Diels-Alder (iEDDA) reactions[29-32]. This strategy has already been successfully employed in the post-synthetic modification of metal-organic cages (MOCs)—for example, to tune the stoichiometry of the assembled cage structure[33] or to direct the partitioning of supramolecular complexes between phases[34]. Moreover, tetrazine moieties exhibit redox activity and strong fluorescence, offering significant potential for applications in both biology and materials science fields[35-38].

In this work, we investigated the use of S_NAr reactions to incorporate tetrazine groups into a chemically stable cage that exhibit permanent porosity in the solid state (Figure 1a). More importantly, the resulting tetrazine POC can undergo further modification via highly efficient iEDDA reations, enabling fine-tuning of its structure or the construction of more advanced architectures.

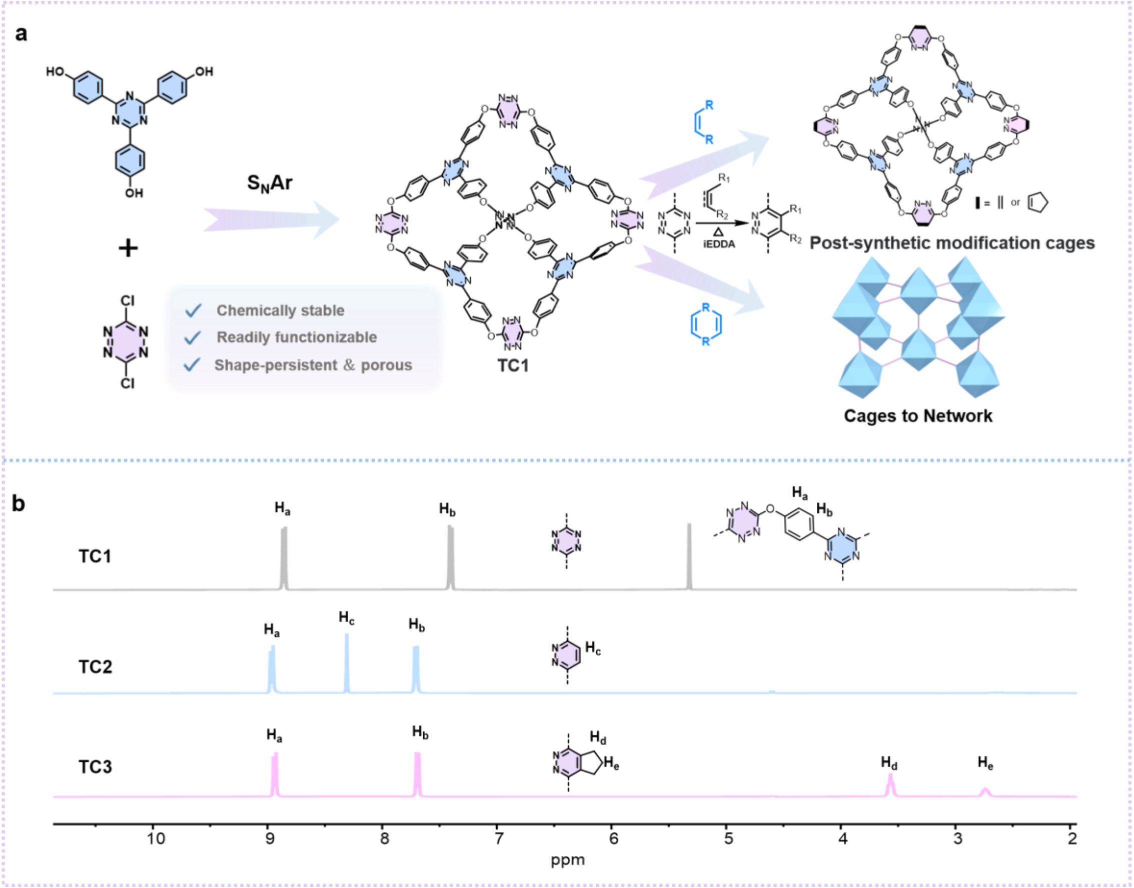

Figure 1. (a) Schematic diagram of the synthesis and post-synthetic modification of **TC1**. (b) The ^{1}H NMR spectra of **TC1**, **TC2** and **TC3** (*d*-TFA, 400 MHz, 298 K).

RESULTS AND DISCUSSION

The synthesis and characterization of TC1. We selected 4,4′,4"-(1,3,5-triazine-2,4,6-triyl) triphenol (TTP) as the building block for POC synthesis due to the excellent conjugation between the triazine core and its substituted benzene rings, which imparts TTP with good planarity and rigidity. TTP was efficiently synthesis from 4-hydroxybenzonitrile using trifluoromethanesulfonic acid as the catalyst. Subsequently, a S_NAr reaction was carried out between 3,6-dichloro-1,2,4,5-tetrazine and TTP under basic conditions. Upon optimizing the reaction conditions (Table S1), we found that a mixed solvent mixture of tetrahydrofuran (THF) and acetonitrile (3:2), in the presence of *N*, *N*-diisopropylethylamine (DIPEA), yielded a product exhibiting intense orange-yellow fluorescence in solution. The ^{1}H NMR spectrum of the reaction product displayed two doublets at 8.85 and 7.40 ppm, which we assigned to the aromatic protons H_a and H_b of the resulting cage product (Figure 1b and Figure S21). Compared with the original ligand (Figure S20), these signals showed significant downfield shifts, likely due to enhanced conjugation upon formation of the highly symmetric cage structure. In the ^{13}C NMR spectrum, two characteristic signals were observed in the range of 171.2-168.2 ppm (Figure S21), corresponding to the carbon atoms of the triazine and tetrazine rings. The relatively simple ^{1}H NMR spectrum also indicated a high degree of symmetry for the cage in solution. The FT-IR spectrum displayed distinct peaks corresponding to aromatic skeletal vibrations and ether bond stretching (Figure S22). To further verify the structure, high-resolution matrix-assisted laser desorption/ionization time-of-flight (MALDI-TOF) mass spectrometry was performed. An ion peak at m/z 1898.438 was observed, matching the theoretical value of 1898.436 for $[[4+6] \text{ cage} + H]^+$ (Figure S5). Single crystals suitable for single-crystal X-ray diffraction (SC-XRD) were obtained by slow evaporation of a dichloromethane/acetone solution (Figure 2a). SC-XRD analysis revealed that the product, designated **TC1**, crystallized in a triclinic system (space group $P\overline{1}$) with a tetrahedral symmetric topology. In this structure, tetrazine units occupy the six vertices of the cage, while TTP units define the four triangular faces. Each edge of the **TC1** cage measures approximately 1.5 nm, with a top-to-bottom vertex distance of 2.2 nm (Figure S23). Four triangular windows, each about 1.4 nm in edge length, provide access to the cage interior.

The crystal structure shows that adjacent **TC1** cages are closely packed through π-π stacking and hydrogen bonding interactions (Figure 2e). These interactions link the cage cavities via the windows, forming interconnected channels along the a, b, and c crystallographic axes (Figure 2f, Figure S24 and S25). Notably, **TC1** shares a similar geometric configuration with one of the representative imine cages, **CC3** (Figure 2d), as both adopt regular octahedral structure. However, the triangular windows in TC1 are considerably larger than those in **CC3**, making **TC1** and its derivatives effectively enlarged analogues of **CC3**. Despite this structural similarity, their solid-state packing differs markedly. In **TC1**, the large, planar TTP units facilitie efficient π-π stacking and hydrogen bonding between adjacent cages. In contrast, **CC3**'s cyclohexanediamine units introduce steric hindrance, limit face-to-face π-π stacking interactions. Instead, **CC3** adopts a window-to-window packing modes primarily by van der Waals forces, which preventing slippage between cages and contributes to its packing stability.

Post-synthetic modification of TC1. Post-synthetic modification of **TC1** was achieved via an iEDDA reaction with tetrazines. Norbornadiene and 1-morpholino-1-cyclopentene are commonly employed dienophiles in such reactions and are well-suited for the post-synthetic modification of tetrazine-containing derivatives. As shown in Fig. 1a (Scheme S3 and S4), two PSM POCs, designated as **TC2** and **TC3**, were successfully synthesized by reacting **TC1** with norbornadiene and 1-monocarbonyl-1-cyclopentene, respectively. The reactivity of the two alkenes was found to differ significantly: **TC1** reacted with norbornadiene only under reflux in 1,4-dioxane and with a large excess of the alkene, while it reacted with 1-morpholino-1-cyclopentene under equimolar conditions at 60 °C. Following synthesis, **TC2** and **TC3** were purified via silica gel column chromatography, yielding final product recoveries of 48.8% and 30.4%, respectively. The structures of **TC2** and **TC3** were confirmed by NMR spectroscopy and MALDI-TOF mass spectrometry. Compared to **TC1**, the ^{1}H NMR spectrum of **TC2** showed the appearance of a new set of aromatic protons signals H_c, indicative of the tetrazine-to-pyridazine ring transformation (Figure 1b). For **TC3**, two additional sets of proton signals (H_d and H_e) were observed, corresponding to aliphatic protons on the cyclopentene ring (Figure 1b). Furthermore, the ^{13}C NMR spectra revealed a significant upfield shift of the carbon signal at position f in both **TC2** and **TC3**, consistent with the ring transformation (Figure S26). MALDI-TOF mass spectrometry of **TC2** and **TC3** displayed ion peaks at m/z 1885.887 (Figure S8) and 2125.794 (Figure S11), respectively, closely matching the calculated values for for $[[4+6] \text{ cages} + H]^+$ (1885.486 for **TC2** and 2125.673 for **TC3**), confirming the successful formation of the target molecular cages.

Comparative analysis of the crystal structures of TC1, TC2, and TC3. Similarly, single crystals of **TC2** suitable for SC-XRD analysis were obtained by slow evaporation of its THF solution. SC-XRD data revealed that **TC2** crystallizes in a monoclinic crystal system with space group $C2/c$, where the cages are closely packed through π-π stacking and hydrogen bonding interactions (Figure S27). Similarly, single crystals of **TC3** were obtained by the room-temperature evaporation of a mixed solvent of DCM and acetone. SC-XRD analysis showed that **TC3** also adopts a monoclinic system, but with space group $P2_1/n$, and exhibits dense cage packing facilitated by π-π stacking and hydrogen bonding (Figure S28).

In comparison to **TC1**, **TC2** and **TC3** exhibit a notable reduction in structural symmetry (Figure 2b/2c), which indirectly leads to distortion of their triangular windows and a decrease in cavity size. This is likely attributed to increased ring strain introduced during post-synthetic modification. The relative degree of distortion in the ether bonds and overall molecular framework can be assessed by examining the dihedral angles between the tetrazine or pyridazine rings and the adjacent benzene rings, as well as the line-plane angles formed by the C-O bond on the benzene ring and the tetrazine or pyridazine ring. Two regions of significant distortion were identified in both **TC2** and **TC3** (Figure S29-S31). At the corresponding positions in **TC1**, the dihedral angle is 81.9°, with a line-plane angle of 2.2°. In contrast, **TC2** displays a dihedral angle of 69.1° and a line-plane angle of 18.4°, while **TC3** exhibits values of 57.7° and 28.8°, respectively. From the perspective of solid-state packing, these distortion in **TC2** and **TC3** result in denser molecular arrangements, leading to smaller cavities and narrower channels along the a, b, and c axes (Figure S32-S35). Thus, pore size can be effectively tuned in this series of cages through post-synthetic modification. Additionally, **TC2** and **TC3** show stronger π-π interactions and hydrogen bonding with adjacent molecules compared to **TC1**. It is noteworthy that in **TC2**, π-π interactions were observed not only between adjacent TTP planes but also between neighboring pyridazine rings (Figure S27). In **TC3**, π-π interactions can further be identified between the pyridazine ring and the benzene ring on the TTP plane of adjacent molecules (Figure S28). This enhancement in intermolecular interactions arises from molecular distortion, which improves complementarity and facilitates multiple π-π stacking interactions.

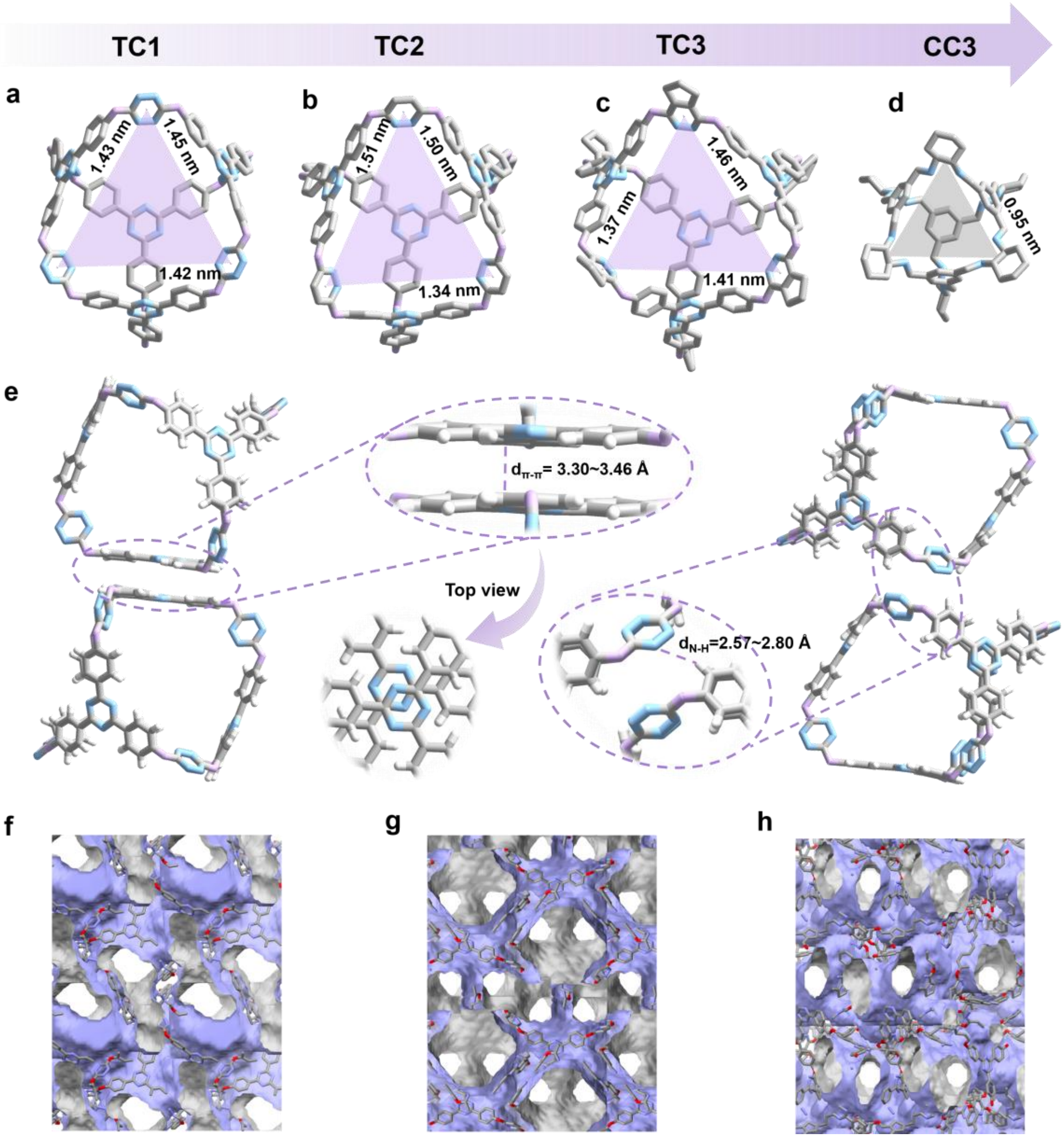

Figure 2. (a) (b) (c) (d) Crystal structures of **TC1**, **TC2, TC3** and **CC3**. (e) Illustration of the π-π stacking and other intermolecular interactions of **TC1** in its single crystal structure. (f) (g) (h) Crystalline voids represented as contact surface (violet outer surface, grey inner surface, created by *Mercury* with a probe radius of 1.82 Å and a grid spacing of 0.5 Å) showing isolated pores.

Chemical stability of TC1, TC2, and TC3. Interestingly, **TC1**, **TC2**, and **TC3** can all be readily obtained as crystalline solids through room temperature evaporating of its solution, indicating that these cages are sufficiently rigid and inherently prone to form ordered structures (Figure S36). More importantly, as shown in Figure 3c, the PXRD diffraction patterns and intensities of **TC1**, **TC2**, and **TC3** remained unchanged before and after solvent removal, demonstrating that their molecular packing is stable upon desolvation. Furthermore, the experimental PXRD patterns closely match the simulated patterns from single-crystal data, further confirming the excellent shape-persistence of the three cage structures. This is noteworthy, as porous molecular crystals typically suffer from structural collapse or loss of crystallinity upon solvent removal. The observed stability in their packing arrangements may be attributed to the strain within the cage structures arising from favorable ether bond angles, the intrinsic rigidity of the ligands, and strong intermolecular interactions, such as π-π stacking between adjacent molecules. Particularly, in their structures, the lone pairs of electrons on the ether-bonded oxygen atom engage in p-π conjugation with adjacent aromatic rings. This conjugation induces a near-sp^2 hybridization at the oxygen center, evidenced by bond angles approaching 120°. The resulting molecular planarity restricts rotation around the ether linkage, while the extended π-conjugation enhances structural rigidity and stability through delocalization of electron density.

POCs constructed with ether linkages are generally expected to exhibit superior chemical stability compared to those formed via dynamic bonds such as imines or boronic esters. To rigorously assess the chemical stability of these cages, **TC1**, **TC2**, and **TC3** were immersed in extreme chemical environments, including boiling water and strong acidic and basic solutions. As shown in Figure 3b, after stirring in these conditions for two days, the ^{1}H NMR spectrum of **TC1** remained unchanged (Figure 3a), indicating good stability in boiling water, concentrated HCl solutions (pH = 0), and NaOH solutions (pH = 12). Notably, the chemical stability of **TC1** surpassed that of many previously reported robust POCs, such as PB-1[39] and FT-RCC3[19] (Figure 3b). However, in stronger alkaline solutions, **TC1** begins to degrade gradually, likely due to nucleophilic attack by OH^- on the tetrazine ring, leading to ring opening and decomposition (Figure S37). After post-synthetic modification, **TC2** and **TC3** exhibit even greater chemical stability. When subjected to highly acidic (12 M HCl) or basic (15 M NaOH) environments for two days, their ^{1}H NMR spectra showed no noticeable changes (Figure 3a). Remarkably, the chemical stability of **TC2** and **TC3** exceeds that of most previously reported stable POCs, such as PAC-1-S[40] and TpOMe-CDA[41], and is comparable to the most chemically stable POCs to date, such as sp^2-POC1[15]. This demonstrates that the PSM strategy can further enhance the durability of **TC1** by reinforcing its more vulnerable components—specifically, the tetrazine units—thus positioning **TC2** and **TC3** among the top tier of chemically robust porous organic cages.

The gas adsorption properties of TC1, TC2, and TC3. The structural rigidity and inherent porosity of **TC1**, **TC2**, and **TC3** motivated us to investigate their gas adsorption properties. N_2 adsorption experiments at 77 K were conducted to evaluate the porosity the activated samples. As shown in Figure 3d, **TC1** and **TC2** exhibit typical Type I adsorption isotherms, indicative of microporous materials. In contrast, **TC3** displays a two-step adsorption behavior (Figure 3d), which we attribute to its smaller and more irregular pore structure. A similar trend was observed in the CO_2 adsorption isotherm of **TC3** at 195 K (Figure S43). The adsorption rapidly approaches saturation at low pressure and then increases sharply with further pressure increases. This behavior may be explained by the initial occupation of external pores by CO_2 molecules at low pressure, followed by delayed penetration into internal pores at higher pressure. Based on the BET model (Figure S44-S47), the Brunauer-Emmett-Teller (BET) surface area of **TC1**, **TC2**, and **TC3** were calculated to be 1157 $m^2\ g^{-1}$, 670 $m^2\ g^{-1}$, and 666 $m^2\ g^{-1}$, respectively. The lower surface areas of **TC2** and **TC3** may be attributed to the distortion of the PSM cages structures and denser packing of the cages, which likely result in narrower pore channels and reduced accessible surface area.

TC1, with its high porosity and multiple triazine and tetrazine moieties, possesses an overall electron-deficient cavity (Figure S48). The electron-deficient nature of the tetrazine groups is expected to enhance the material’s affinity for SF_6, a gas that is highly polarizable and carries a partial negative charged surface. SF_6 is extensively used as an insulating gas in high-voltage electrical equipment and as a protective gas in the semiconductor industry because of its excellent dielectric and arc-quenching properties. However, its global warming potential is more than 20,000 times that of CO_2, making its capture and separation an increasingly important target. We therefore investigated the SF_6 adsorption performance of **TC1**. As shown in Figure 3e, **TC1** adsorbs 2.59 mmol g^{-1} of SF_6 at 298 K and 1 bar, increasing to 3.05 mmol g^{-1} at 273 K. These values outperforms most other organic porous materials—such as CC3[42], BrCOF-2-CF_3[43], PAF-XJTU-1[44]—in SF_6 adsorption under comparable conditions. Similarly, the high CO_2 uptake observed for **TC1** (Figure S49 and Table S2) may also be attributed to the electron-deficient sites in the cage interacts favorably with the polarizable CO_2 gases. We also investigated the SF_6 adsorption capacity of **TC2** and **TC3**, which lack tetrazine functional groups. At 298 K and 1 bar, **TC2** and **TC3** adsorbed 1.20 mmol g^{-1} and 1.02 mmol g^{-1} of SF_6, respectively (Figure S50-S53). Compared to **TC1**, both PSM cages exhibited significantly lower SF_6 adsorption capacities. The reduction is likely due to the conversion of tetrazine groups to pyridazine groups in **TC2** and **TC3**, combined with their reduced porosity—both factors contributing to the diminished SF_6 adsorption capacities.

To evaluate the binding affinity between **TC1** and the adsorbates, the isosteric heat of adsorption (Q_{st}) of SF_6 and N_2 on **TC1** was calculated using the Clausius-Clapeyron equation[45] based on single-component adsorption isotherms at 298 K and 273 K. At zero coverage, **TC1** exhibited a Q_{st} 22.1 kJ mol^{-1} for SF_6 and 12.7 kJ mol^{-1} for N_2 (Figure 3f). The higher heat of adsorption for SF_6 indicates stronger interactions with the cage material compared to N_2. The SF_6/N_2 selectivity of **TC1** at 298 K and 1 bar was further evaluated using Ideal Adsorbed Solution Theory (IAST), with adsorption isotherms fitted using the dual-site Langmuir model via *IAST++* software. Under ideal conditions, the IAST selectivity of **TC1** for SF_6/N_2 (10:90) mixture was calculated to be 135 (Figure S54), demonstrating a high preference for SF_6. Notably, at 298 K and 0.1 bar, **TC1** adsorbed 1.17 mmol g^{-1} of SF_6 with an IAST selectivity of 136. This performance is comparable to those reported for leading organic porous materials and some of the best-performing metal-organic frameworks (MOFs)[46], including CC3[42], HKUST-1c[47] and UiO-66[48], etc (More details in Table S3) . To assess the practical separation performance, dynamic breakthrough experiments were conducted using a SF_6/N_2 mixture (1/9, v/v) at a flow rate of 3 mL/min. As shown in Fig. 3g, N_2 eluted rapidly from the **TC1**-packed column at 1 bar, indicating minimal co-adsorption. In contrast, SF_6 exhibited a significantly delayed breakthrough, with a retention time of approximately 30 min g^{-1}, highlighting the strong selective adsorption of SF_6 by **TC1**. Furthermore, after five consecutive breakthrough cycles, the SF_6/N_2 separation performance of **TC1** remained consistent, demonstrating excellent regenerability and cycling stability (Fig. 3g). Finally, PXRD analysis of **TC1**, **TC2**, and **TC3** after gas adsorption confirmed that all three compounds retained good crystallinity and undisturbed solid-state packing throughout the measurements, further verifying the structural stability of the materials (Figure S55-S57).

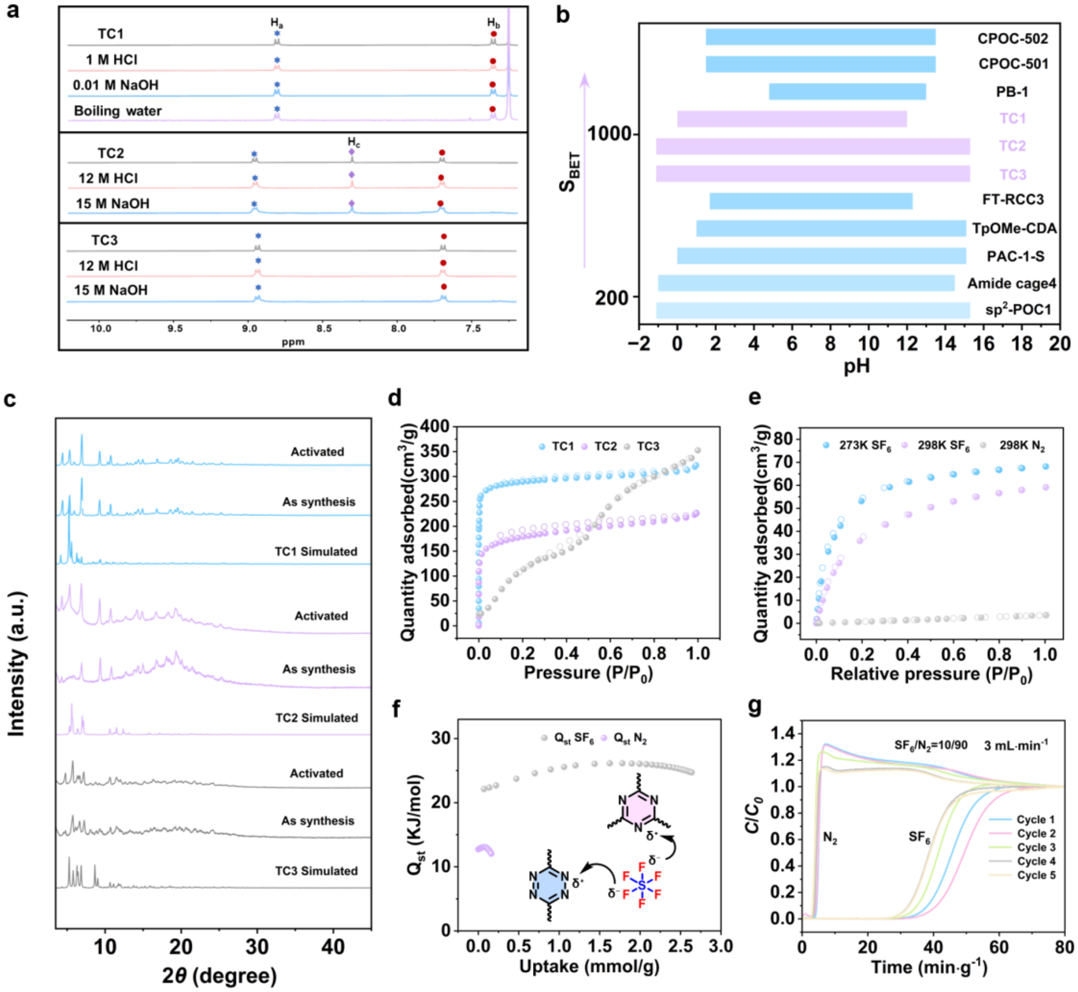

Figure 3. (a) The ^{1}H NMR spectra of **TC1**($CDCl_3$, 400 MHz, 298 K), **TC2** and **TC3** (*d*-TFA, 400 MHz, 298 K) after treatment with different conditions. (b) Comparison of the chemical stability and surface area of **TC1**, **TC2** and **TC3** with that of POCs reported in the study. (c) Comparison of PXRD pattern of **TC1**, **TC2** and **TC3** under various conditions. (d) The sorption isotherms of **TC1, TC2** and **TC3** for N_2 at 77 K. (e) Adsorption isotherm of SF_6 and N_2 by **TC1** at 298 K and 273 K, 1 bar. (f) The isosteric heat of adsorption of **TC1** for SF_6 and N_2 (Inset: Electrostatic interactions between electron-rich surfaces of SF_6 and triazine/tetrazine moieties). (g) SF_6/ N_2 (10: 90) breakthrough curve for **TC1** at 298 K and 1 bar.

Construction of networked materials using TC1 as building block. The promising gas adsorption properties and excellent chemical stability of **TC1** prompted us to explore its potential in constructing advanced architectures. The strategy of using discrete cages as building blocks to assemble extended networks—commonly referred to as the cage-to-framework approach—is particularly appealling[49], as it enables the integration of the advantageous features of both molecular cages and extended frameworks. For instance, using soluble cages as precursors for the construction of three-dimensional covalent organic frameworks (COFs) can incorporate cage cavities into the framework and improve gas separation selectivity[22]. In this study, **TC1** was employed as the building block for framework construction via the iEDDA reaction. Alkenes-based linkers with two double bonds and intrinsic ring strain were selected to facilitate efficient linkage formation. Specifically, trans-cyclooctene (*E*-COD) and norbornene (NBD) derivatives, which are widely used in iEDDA chemistry, were chosen. Accordingly, trans-cyclooctadiene (*E*, *E*-COD) and the dimer of norbornene (NBD2) was synthesized following literature procedures[50, 51]. Reaction between **TC1** and *E*, *E*-COD, or with NBD2, was carried out using a mixture of dimethylformamide (DMF) and dichloromethane (DCM) or acetonitrile (ACN) as solvent, respectively (Fig. 4a). As the reaction progressed, the solution color changed from orange-red to colorless or pale yellow, accompanied by continuous gas evolution (N_2 releasing) and the formation of insoluble solids (Figure S58). These observations indicate the successful formation of assembled materials-designated **TC1-P1** (from *E*, *E*-COD) and **TC1-P2** (from NBD2), respectively. Notably, a difference in reactivity was observed: the reaction between **TC1** and *E*, *E*-COD proceeded readily at room temperature, while the reaction with NBD2 requires elevated temperatures. This discrepancy is likely due to the greater ring strain in *E*, *E*-COD, which facilitates the iEDDA reaction more efficiently. Despite successful formation of the products, PXRD analysis revealed no long-rang order in the resulting materials. We attribute this lack of crystallinity to two main factors: first, the iEDDA reaction is rapid and irreversible under the investigated conditions, which restricts the possibility for structural rearrangement and self-correction during assembly; second, significant distortion of the **TC1** cage occurs upon reaction, increasing structural asymmetry. This enhanced asymmetry likely favors the formation of disordered architectures over highly ordered crystalline frameworks. Consequently, these promotes the formation of relatively disordered structures.

The solid-state NMR spectra of the reaction products are shown in Fig. 4b. Compared to **TC1**, the carbon signals labeled f' in **TC1-P1** and **TC1-P2** were exhibited high-field shift. Additionally, a new set of resonances emerged, which we attributed to the carbon atom g in the newly formed pyridazine ring. These observations are consistent with theoretical expectations, confirming that the iEDDA reaction proceeded as intended and the target products were successfully obtained. Further evidence supporting product formation was provided by FT-IR spectroscopy. Compared to **TC1**, **TC1-P1** and **TC1-P2** exhibited new absorption bands. In particular, the peaks at 2832 and 2943 cm^{-1} correspond to the stretching vibrations of the methylene group on the cyclooctadiene, indicative of successful covalent linkage formation (Figure S59). In addition to structural confirmation, thermal gravimetric analysis (TGA) revealed enhanced thermal stability in the networked products (Figure S60 and S61).

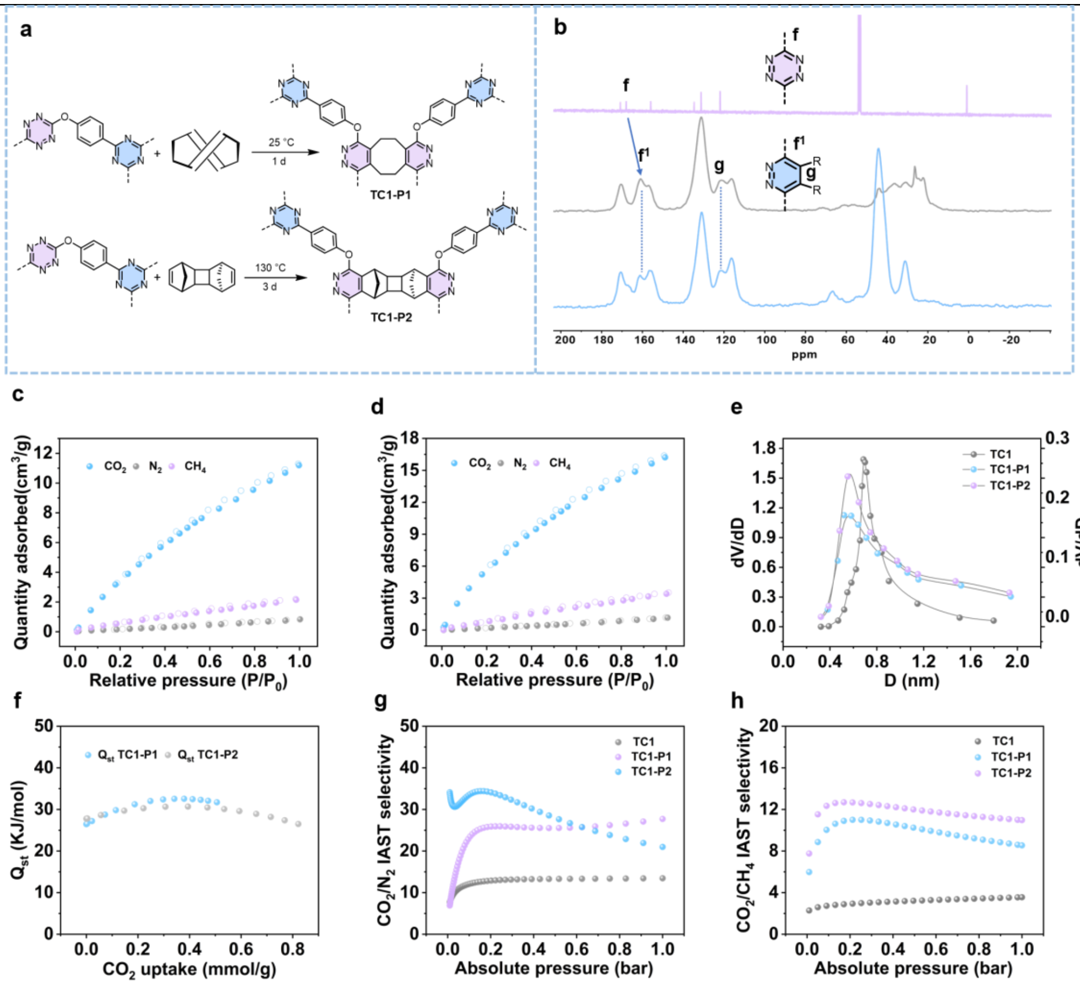

Figure 4. (a) The synthesis scheme for **TC1-P1** and **TC1-P2**. (b) Solid-state NMR spectra of **TC1-P1** and **TC1-P2**. (c) (d) Adsorption isotherm of CO_2, CH_4 and N_2 by **TC1-P1** and **TC1-P2** at 298 K, 1 bar. (e) Differences in pore size distribution of **TC1**, **TC1-P1**and **TC1-P2**. (f) The isosteric heat of adsorption of **TC1-P1** and **TC1-P2** for CO_2. (g) The CO_2/N_2 selectivity of **TC1**, **TC1-P1** and **TC1-P2** at 298 K, 1 bar. (h) The CO_2/CH_4 selectivity of **TC1**, **TC1-P1**and **TC1-P2** at 298 K, 1 bar.

A preliminary investigation into the gas adsorption behavior of **TC1-P1** and **TC1-P2** was conducted. After solvent removal, their porosity and permanent pore volume were evaluated using N_2 adsorption measurements at 77K. As shown in Figure S62-S65, both **TC1-P1** and **TC1-P2** exhibited negligible N_2 uptake, suggesting a significant reduction in pore size following framework formation. To further assess their porosity, CO_2 adsorption measurements were performed at 195 K. The results revealed relatively low CO_2 uptake, with BET surface areas to be 263.7 m^2 g^{-1} for **TC1-P1** and 310.4 m^2 g^{-1} for **TC1-P2** (Figure S66-S69). This reduction in surface area and gas uptake is likely due to increased cross-linking during network formation, which result in a denser structure and narrower pore sizes (Figure 4e). The gas adsorption capacities of **TC1-P1** and **TC1-P2** for CO_2, CH_4 and N_2 were also evaluated at 298 K and 273 K (Figure S70 and S71). At 298 K and 1 bar, **TC1-P1** adsorbed 0.51mmol g^{-1} of CO_2, 0.10 mmol g^{-1} of CH_4 and 0.04 mmol g^{-1} of N_2 (Figure 4c). In comparison, **TC1-P2** showed slightly higher uptake, with 0.82 mmol g^{-1} of CO_2, 0.15 mmol g^{-1} of CH_4 and 0.05 mmol g^{-1} of N_2 (Figure 4d). The adsorption selectivity of **TC1-P1** and **TC1-P2** was analyzed using IAST at 298K and 1bar. Under ideal conditions, the IAST selectivity of for a CO_2/N_2 (15:85) mixture was calculated to be 27.7 for **TC1-P1**, 21.0 for **TC1-P2**, and only 13.5 for **TC1** (Figure 4g). For the CO_2/CH_4 (50:50) mixture, **TC1-P1** and **TC1-P2** exhibited selectivities of 8.5 and 11.0, respectively, while **TC1** was only 3.5 (Figure 4h). Although the post-synthetic modification led to a decrease in overall CO_2 and CH_4 uptake compared to the parent cage **TC1**, the IAST selectivity for both CO_2/N_2 and CO_2/CH_4 mixture showed significant enhancement. These findings suggest that the microstructures of the materials can be effectively tuned through PSM strategy to optimize gas separation performance.

CONCLUSION

In summary, we have successfully synthesized a shape-persistent POC, **TC1**, via a one-pot S_NAr reaction. The combination of the intrinsic angularity of ether linkages, the rigidity of the TTP building units, and strong π-π stacking interactions between **TC1** molecules contributes to its excellent structural persistence and porosity in the solid state. The presence of chemically robust ether bonds further imparts **TC1** with outstanding chemical stability. In addition, **TC1** exhibits significant adsorption capacities for SF_6 and CO_2, making it a promising candidate for greenhouse gases capture applications. Furthermore, post-synthetic modification of **TC1** via iEDDA reactions yielded functionalized POCs and cage-based network structures materials. These modified structures demonstrate enhanced chemical robustness, maintaining their integrity even under harsh acidic and basic conditions such as concentrated HCl and NaOH solutions. This study showcases the utility of S_NAr chemistry in constructing chemically robust POCs and highlights the versatility of tetrazine units as reactive handles for post-synthetic modifications, broadening the scope of POC design for advanced applications.

ASSOCIATED CONTENT

The Supporting Information is available free of charge at figures S1–S71, Tables S1-S4. Experimental details; FTIR spectra, PXRD, SC-XRD, gas adsorption analysis and gas separation performance data (PDF).

AUTHOR INFORMATION

Corresponding Author

Ming Liu - *Department of Chemistry Zhejiang University Hangzhou 310027, China & ZJU-Hangzhou Global Scientific and Technological Innovation Center Hangzhou 311215, China*.
E-mail: mingliu@zju.edu.cn

Authors

Ju Yang - *Department of Chemistry Zhejiang University Hangzhou 310027, China.*
Saisai Yu - *Department of Chemistry Zhejiang University Hangzhou 310027, China.*
Wendi Zhang - *Department of Chemistry Zhejiang University Hangzhou 310027, China.*
Dingyue Hu - *ZJU-Hangzhou Global Scientific and Technological Innovation Center Hangzhou 311215, China & Department of Chemistry Zhejiang University Hangzhou 310027, China.*
Yutao Guan - *Department of Chemistry Zhejiang University Hangzhou 310027, China.*

Hongqin Li - *ZJU-Hangzhou Global Scientific and Technological Innovation Center Hangzhou 311215, China & Department of Chemistry Zhejiang University Hangzhou 310027, China.*

Author Contributions

All authors have contributed to the design and implementation of the studies reported here and have given approval to the final version of the manuscript.

Notes

The authors declare no competing financial interest.

ACKNOWLEDGMENT

The authors thank the National Natural Science Foundation of China (22371252), the Zhejiang Provincial Natural Science Fund (LZ23B020005), the Leading Innovation Team grant from Department of Science and Technology of Zhejiang Province (2022R01005). Thanks to Roentgen Laboratory for SC-XRD testing and technical support.

REFERENCES

(1) Yang, X.; Ullah, Z.; Stoddart, J. F.; Yavuz, C. T. Porous Organic Cages. *Chem. Soc. Rev.* **2023**, 123 (8), 4602-4634.

(2) Hasell, T.; Cooper, A. I. Porous Organic Cages: Soluble, Modular and Molecular Pores. *Nat. Rev. Mater.* **2016**, 1 (9), 16053.

(3) Bhat, A. S.; Elbert, S. M.; Zhang, W. S.; Rominger, F.; Dieckmann, M.; Schroder, R. R.; Mastalerz, M. Transformation of a [4+6] Salicylbisimine Cage to Chemically Robust Amide Cages. *Angew. Chem., Int. Ed.* **2019**, 58 (26), 8819-8823.

(4) Mastalerz, M. Porous Shape-Persistent Organic Cage Compounds of Different Size, Geometry, and Function. *Acc. Chem. Res.* **2018**, 51 (10), 2411-2422.

(5) Yu, S. S.; Yang, S. Y; Yang, M.; Yang, J.; Song, Z. Y; Hu, D. Y; Ji, H.; Jia, Z.; Liu, M. Regularly Arranged Heterogeneous Pores in Gas Separation Membranes Constructed by Cocrystallization of Porous Organic Molecules. *Angew. Chem., Int. Ed.* **2025**, 64 (7), e202420086.

(6) Liu, C.; Liu, K.; Wang, C.; Liu, H.; Wang, H.; Su, H.; Li, X.; Chen, B.; Jiang, J. Elucidating Heterogeneous Photocatalytic Superiority of Microporous Porphyrin Organic Cage. *Nat. Commun.* **2020**, 11 (1), 1047.

(7) Hussain, M. D. W.; Giri, A.; Patra, A. Organic Nanocages: A Promising Testbed for Catalytic CO_2 Conversion. *Sustain. Energy Fuels*. **2019**, 3 (10), 2567-2571.

(8) Liu, M.; Zhang, L.-D.; Little, M.-A.; Kapil, V.; Ceriotti, M.; Yang, S.-Y.; Holden, D. L.; He, D.-L.; Clowes, R.; et al. Barely Porous Organic Cages for Hydrogen Isotope Separation. *science*. **2019**, 366 (6465), 613-620.

(9) Tozawa, T.; Jones, J. T.; Swamy, S. I.; Jiang, S.; Adams, D. J.; Shakespeare, S.; Clowes, R.; Bradshaw, D.; Hasell, T.; Chong, S.-Y.; et al. Porous Organic Cages. *Nat. Mater.* **2009**, 8 (12), 973-978.

(10) Su, K.; Wang, W.; Du, S.; Ji, C.; Zhou, M.; Yuan, D. Reticular Chemistry in the Construction of Porous Organic Cages. *J. Am. Chem. Soc.* **2020**, 142 (42), 18060-18072.

(11) Sun, Z.; Li, P.; Xu, S.; Li, Z. Y.; Nomura, Y.; Li, Z.; Liu, X.; Zhang, S. Controlled Hierarchical Self-Assembly of Catenated Cages. *J. Am. Chem. Soc.* **2020**, 142 (24), 10833-10840.

(12) Zhang, G.; Presly, O.; White, F.; Oppel, I. M.; Mastalerz, M. A Permanent Mesoporous Organic Cage with an Exceptionally High Surface Area. *Angew. Chem., Int. Ed.* **2014**, 53 (6), 1516-1520.

(13) Andrews, K. G.; Piskorz, T. K.; Horton, P. N.; Coles, S. J. Enzyme-like Acyl Transfer Catalysis in a Bifunctional Organic Cage. *J. Am. Chem. Soc.* **2024**, 146 (26), 17887-17897.

(14) Yang, J.; Shi, R.; Mao, L.-L.; Xiao, H.; Zeng, Y.; Liao, G.; Weng, Y.; Li, X.-B.; Zhao, J.; Zhao, Y.; et al. Photoinduced Intramolecular Charge Transfer in Strained Organic Cage Containing Orthogonally Arranged Donors and Acceptors. *CCS Chem.* **2024**, 6 (8), 1920-1928.

(15) Qiu, F.; Chen, X.; Wang, W.; Su, K.; Yuan, D. Highly Stable sp^2 Carbon-Conjugated Porous Organic Cages. *CCS Chem.* **2024**, 6 (1), 149-156.

(16) Yue, M. S.; Luo, N.; Wang, X. D.; Ao, Y. F.; Wang, D. X.; Wang, Q. Q. Cooperative Anion-pi Catalysis with Chiral Molecular Cages toward Enantioselective Desymmetrization of Anhydrides. *J. Am. Chem. Soc.* **2025**, 147 (3), 2303-2308.

(17) Zhou, H.; Ao, Y. F.; Wang, D. X.; Wang, Q. Q. Inherently Chiral Cages via Hierarchical Desymmetrization. *J. Am. Chem. Soc.* **2022**, 144 (37), 16767-16772.

(18) Zhu, Q.; Qu, H.; Avci, G.; Hafizi, R.; Zhao, C.; Day, G. M.; Jelfs, K. E.; Little, M. A.; Cooper, A. I. Computationally Guided Synthesis of a Hierarchical [4[2+3]+6] Porous Organic 'Cage of Cages'. *Nat. Synth.* **2024**, 3 (7), 825-834.

(19) Liu, M.; Little, M. A.; Jelfs, K. E.; Jones, J. T.; Schmidtmann, M.; Chong, S. Y.; Hasell, T.; Cooper, A. I. Acid- and Base-Stable Porous Organic Cages: Shape Persistence and pH Stability via Post-synthetic "Tying" of a Flexible Amine Cage. *J. Am. Chem. Soc.* **2014**, 136 (21), 7583-7586.

(20) Bhat, A. S.; Elbert, S. M.; Zhang, W. S.; Rominger, F.; Dieckmann, M.; Schröder, R. R.; Mastalerz, M. Transformation of a [4+6] Salicylbisimine Cage to Chemically Robust Amide Cages. *Angew. Chem., Int. Ed.* **2019**, 58 (26), 8819-8823.

(21) Wu, W.; Chen, D.; Zhang, M.; Zhao, X.; Zhao, R.; Geng, C.; Jia, J.; Zhu, G. Uranium Extraction from Seawater via Hydrogen Bond Porous Organic Cages. *J. Am. Chem. Soc.* **2025**, 147 (2), 2228-2236.

(22) Zhu, Q.; Wang, X.; Clowes, R.; Cui, P.; Chen, L.; Little, M. A.; Cooper, A. I. 3D Cage COFs: A Dynamic Three-Dimensional Covalent Organic Framework with High-Connectivity Organic Cage Nodes. *J. Am. Chem. Soc.* **2020**, 142 (39), 16842-16848.

(23) Zhang, C.; Wang, Z.; Tan, L.; Zhai, T. L.; Wang, S.; Tan, B.; Zheng, Y. S.; Yang, X. L.; Xu, H. B. A Porous Tricyclooxacalixarene Cage Based on Tetraphenylethylene. *Angew. Chem., Int. Ed.* **2015**, 54 (32), 9244-9248.

(24) Wang, D. X.; Wang, M. X. Exploring Anion-pi Interactions and Their Applications in Supramolecular Chemistry. *Acc. Chem. Res.* **2020**, 53 (7), 1364-1380.

(25) Wang, X.-D.; Wang, D.-X.; Huang, Z.-T.; Wang, M.-X. One-pot Synthesis of Oxygen and Nitrogen-Bridged Calix[2]arene[2]triazines. *Supramol. Chem*. **2014**, 26 (7-8), 601-606.

(26) Jeffrey L. Katz, K. J. S., and Rebecca R. Conry. Single-Step-Synthesis-of-D_{3h}-Symmetric-Bicyclooxacalixarenes. *Org. Lett*. **2005**, 7(16), 3505-3507.

(27) Zhang, C.; Wang, Z.; Tan, L.; Zhai, T. L.; Wang, S.; Tan, B.; Zheng, Y. S.; Yang, X. L.; Xu, H. B. A Porous Tricyclooxacalixarene Cage Based on Tetraphenylethylene. *Angew. Chem., Int. Ed.* **2015**, 54 (32), 9244-9248.

(28) Santos, T.; Rivero, D. S.; Perez-Perez, Y.; Martin-Encinas, E.; Pasan, J.; Daranas, A. H.; Carrillo, R. Dynamic Nucleophilic Aromatic Substitution of Tetrazines. *Angew. Chem., Int. Ed.* **2021**, 60 (34), 18783-18791.

(29) Fu, Z. D.; Guo, Q. H.; Zhao, L.; Wang, D. X.; Wang, M. X. Synthesis and Structure of Corona[6](het)arenes Containing Mixed Bridge Units. *Org. Lett*. **2016**, 18 (11), 2668-2671.

(30) Lu, Y.; Fu, Z. D.; Guo, Q. H.; Wang, M. X. O_6-Corona[6]arenes with Expanded Cavities for Specific Complexation with C_{70}. *Org. Lett*. **2017**, 19 (7), 1590-1593.

(31) Knall, A. C.; Slugovc, C. Inverse electron demand Diels-Alder (iEDDA)-initiated conjugation: a (high) potential click chemistry scheme. *Chem. Soc. Rev.* **2013**, 42 (12), 5131-5142.

(32) Tang, H.; Zhang, H.-N.; Gao, X.; Zou, Y.; Jin, G.-X. The Topological Transformation of Trefoil Knots to Solomon Links via Diels-Alder Click Reaction. *J. Am. Chem. Soc.* **2024**, 146 (23), 16020-16027.

(33) Black, M. R.; Bhattacharyya, S.; Argent, S. P.; Pilgrim, B. S. Structural Transformations of Metal-Organic Cages through Tetrazine-Alkene Reactivity. *J. Am. Chem. Soc.* **2024**, 146, 41, 28233–28241.

(34) Pilgrim, B. S.; Roberts, D. A.; Lohr, T. G.; Ronson, T. K.; Nitschke, J. R. Signal Transduction in a Covalent Post-assembly Modification Cascade. *Nat. Chem.* **2017**, 9 (12), 1276-1281.

(35) Liu, L.; Zhang, D.; Johnson, M.; Devaraj, N. K. Light-activated Tetrazines Enable Precision Live-cell Bioorthogonal Chemistry. *Nat. Chem.* **2022**, 14 (9), 1078-1085.

(36) Yu, A.; He, X.; Shen, T.; Yu, X.; Mao, W.; Chi, W.; Liu, X.; Wu, H. Design Strategies for Tetrazine Fluorogenic Probes for Bioorthogonal Imaging. *Chem. Soc. Rev.* **2025**, 54, 2984-3016.

(37) Zadehnazari, A.; Khosropour, A.; Altaf, A. A.; Rosen, A. S.; Abbaspourrad, A. Tetrazine-Linked Covalent Organic Frameworks with Acid Sensing and Photocatalytic Activity. *Adv. Mater.* **2024**, 36 (14), e2311042.

(38) Li, N.; Zhang, J.; Xie, X.; Wang, K.; Qi, D.; Liu, J.; Lan, Y. Q.; Jiang, J. 3D N-heterocyclic Covalent Organic Frameworks for Urea photosynthesis from NH_3 and CO_2. *Nat. Commun.* **2025**, 16 (1), 1106.

(39) Hong, S.; Rohman, M. R.; Jia, J.; Kim, Y.; Moon, D.; Kim, Y.; Ko, Y. H.; Lee, E.; Kim, K. Porphyrin Boxes: Rationally Designed Porous Organic Cages. *Angew. Chem., Int. Ed.* **2015**, 54 (45), 13241-13244.

(40) Cui, D. X.; Geng, Y.; Kou, J. N.; Shan, G. G.; Sun, C. Y.; Zhang, K. H.; Wang, X. L.; Su, Z. M. Chiral Self-sorting and Guest Recognition of Porous Aromatic Cages. *Nat. Commun.* **2022**, 13 (1), 4011.

(41) Bera, S.; Dey, K.; Pal, T. K.; Halder, A.; Tothadi, S.; Karak, S.; Addicoat, M.; Banerjee, R. Porosity Switching in Polymorphic Porous Organic Cages with Exceptional Chemical Stability. *Angew. Chem., Int. Ed.* **2019**, 58 (13), 4243-4247.

(42) Hasell, T.; Miklitz, M.; Stephenson, A.; Little, M. A.; Chong, S. Y.; Clowes, R.; Chen, L.; Holden, D.; Tribello, G. A.; Jelfs, K. E.; et al. Porous Organic Cages for Sulfur Hexafluoride Separation. *J. Am. Chem. Soc.* **2016**, 138 (5), 1653-1659.

(43) Liao, Q.; Ke, C.; Huang, X.; Wang, D.; Han, Q.; Zhang, Y.; Zhang, Y.; Xi, K. A Versatile Method for Functionalization of Covalent Organic Frameworks via Suzuki-Miyaura Cross-Coupling. *Angew. Chem., Int. Ed.* **2020**, 60 (3), 1411-1416.

(44) Wu, Y.; Li, X.; Li, Y.; Tao, C.; Tang, Y.; Wang, S.; Fu, Y.; Ma, W.; Zhang, W.; Ma, H. Porous Aromatic Frameworks as HF Resistant Adsorbents for SF_6 Separation at Elevated Pressure. *Sep. Purif. Technol.* **2023**, 315, 13657.

(45) Kou, J.-N.; Cui, D.-X.; Jiang, J.-Z.; Li, W.-L.; Shan, G.-G.; Wang, H.; Wang, X.-L.; Su, Z.-M.; Sun, C.-Y. Organic Cage with Interconnected Aromatic Cavity-Channel Pores for One-Step Purification of Ethylene. Adv. Funct. Mater. **2025**, 2501580.

(46) Chuah, C. Y.; Lee, Y.; Bae, T.-H. Potential of Adsorbents and Membranes for SF_6 Capture and Recovery: A review. *Chem. Eng. J.* **2021**, 404, 126577.

(47) Chuah, C. Y.; Goh, K.; Bae, T.-H. Hierarchically Structured HKUST-1 Nanocrystals for Enhanced SF_6 Capture and Recovery. *J. Phys. Chem. C*. **2017**, 121 (12), 6748-6755.

(48) Kim, M.-B.; Kim, K.-M.; Kim, T.-H.; Yoon, T.-U.; Kim, E.-J.; Kim, J.-H.; Bae, Y.-S. Highly Selective Adsorption of SF_6 over N_2 in a Bromine-Functionalized Zirconium-Based Metal-organic Framework. *Chem. Eng. J.* **2018**, 339, 223-229.

(49) Huang, S.; Teat, S. J.; Wayment, L. J.; Settineri, N. S.; Chen, H.; Lei, Z.; Zhang, W. Single-Crystal Cage Framework with High Selectivity and Reversibility in Fullerene Binding. *Angew. Chem., Int. Ed.* **2024**, 63 (38), e202409432.

(50) Stöckmann, H.; Neves, A. A.; Day, H. A.; Stairs, S.; Brindle, K. M.; Leeper, F. J. (E, E)-1,5-Cyclooctadiene: A Small and Fast Click-Chemistry Multitalent. *Chem. Commun.* **2011**, 47 (25), 7203-7205.

(51) Bischoff, D. J.; Lee, T.; Kang, K.-S.; Molineux, J.; O'Neil Parker, W.; Pyun, J.; Mackay, M. E. Unraveling the Rheology of Inverse Vulcanized Polymers. *Nat. Commun.* **2023**, 14 (1), 7553.